

**The History of the University of Wisconsin
Atmospheric Emitted Radiance
Interferometer (AERI) Prototype During
the Period April 1994 Through July 1995**

June 1999

(Manuscript received November 1995,
in final form December 1995)

R. Knuteson
B. Whitney
H. Revercomb
F. Best

Prepared by the Space Science and Engineering Center,
University of Wisconsin - Madison

Work supported by the U.S. Department of Energy,
Office of Energy Research, Office of Health and Environmental Research

Abstract

This document describes reprocessing of data collected with the University of Wisconsin (UW) Atmospheric Emitted Radiance Interferometer (AERI) prototype at the U.S. Department of Energy Atmospheric Radiation Measurement (ARM) Program's Southern Great Plains (SGP) Cloud And Radiation Testbed Central Facility (CART CF) during the period April 1994 through July 1995. Two corrections have been applied to the downwelling atmospheric radiance observed by the AERI prototype during the period April 11, 1994, through April 28, 1995. The first is a small calibration refinement that accounts for an improved characterization of the AERI prototype blackbodies based upon thermal modeling and cavity paint spectral measurements. The second correction was required to remove the effect of an obstruction that was found in the AERI prototype sky field of view. The obstruction caused an error of several percent of ambient radiance, substantially exceeding the AERI calibration uncertainty of less than about 1%. The basis for the sky field of view obstruction correction came from coincident downwelling radiance data of the AERI facility instrument (AERI-01), which was first deployed to the SGP CART CF in April 1995. The obstruction in the AERI prototype was removed on April 28, 1995. The reprocessing of data from the period April 29, 1995, through May 31, 1995, required only the smaller hot blackbody correction. The real-time processing software was modified at that time such that no correction was required for the AERI prototype data beginning June 1, 1995, through the last full day of operation, July 25, 1995. The data corrections described in this document bring the corrected AERI prototype (AERI-00) data in the period April 1994 through July 1995 up to a level of quality comparable to the AERI-01 facility instrument, though with somewhat greater absolute uncertainties.

Contents

Abstract.....	iii
1. Overview	1
1.1 Observations.....	1
1.2 Corrections	1
1.3 Examples	2
1.4 Correction Implementation	2
2. Hot Blackbody Cavity Correction	9
3. Sky Field of View Obstruction Correction.....	14
3.1 Correction.....	15
3.2 Errors.....	18
4. AERI-00 and AERI-01 Comparison.....	32
5. Interactive Data Language Correction Script	36

Figures

1.1	The AERI prototype as it was configured inside the SGP CART CF optical trailer near Billings, Oklahoma.....	4
1.2	Example of a corrected AERI observation (channel 1) for a clear, dry atmosphere (March 10, 1995, 05:30 UTC, SGP CART site near Billings, Oklahoma).....	5
1.3	Example of a corrected AERI observation (channel 2) for a clear, dry atmosphere (March 10, 1995, 05:30 UTC, SGP CART site near Billings, Oklahoma).....	6
1.4	Example of a corrected AERI observation (channel 1) for a clear, moist atmosphere (March 22, 1995, 05:30 UTC, SGP CART site near Billings, Oklahoma).....	7
1.5	Example of a corrected AERI observation (channel 2) for a clear, moist atmosphere (March 22, 1995, 05:30 UTC, SGP CART site near Billings, Oklahoma).....	8
2.1	AERI blackbody cavity cross section.....	12
2.2	Paint emissivity used in AERI blackbodies.....	13
3.1	Average of 17 spectra obtained on April 26, 1995, during the time period 5.7 to 7.9 hours UTC.....	21
3.2	Difference spectra between the two instruments on April 26, 1995, showing the effect of the obstruction.....	22
3.3	Drawing of obstruction effect in beam.....	23
3.4	Calculation of effective obstruction area, \tilde{f}_v , using the AERIPROTO and AERI-01 spectra obtained simultaneously on April 26, 1995, and Eq. (3.14).....	23
3.5	Difference spectra between the two instruments on April 26, 1995, after correcting for the obstruction, using the same data set as in Figure 3.2.....	24
3.6	Difference spectra between the two instruments on May 2, 1995, after the obstruction was physically removed.....	25
3.7a	The calculated correction for April 13, 1994; average of four spectra taken at 14.7 hours UTC.....	26
3.7b	The calculated correction for April 25, 1994; average of four spectra taken at 11.6 hours UTC.....	27

3.7c The calculated correction for August 18, 1994; average of four spectra taken at 20.7 hours UTC 28

3.8a Estimated errors in the correction for April 13, 1994, 14.7 hours UTC..... 29

3.8b Estimated errors in the correction for April 25, 1994, 11.6 hours UTC..... 30

3.8c Estimated errors in the correction for August 18, 1994, 20.7 hours UTC..... 31

4.1 Comparison of coincident longwave channel observations of the AERI prototype (AERI-00) and the AERI CF instrument (AERI-01) obtained at the ARM CART site near Billings, Oklahoma 34

4.2 Comparison of coincident shortwave channel observations of the AERI prototype (AERI-00) and the AERI CF instrument (AERI-01) obtained at the ARM CART site near Billings, Oklahoma 35

Tables

1.1 Milestones in the AERI Prototype Operations from the ARM SGP CART Site..... 1

1. Overview

The purpose of this document is to describe in detail the reprocessing of data collected with the University of Wisconsin (UW) Atmospheric Emitted Radiance Interferometer (AERI) prototype at the U.S. Department of Energy Atmospheric Radiation Measurement (ARM) Program's Southern Great Plains (SGP) Cloud And Radiation Testbed Central Facility (CART CF) during the period April 11, 1994, through July 25, 1995.

1.1 Observations

On March 15, 1993, the UW deployed an AERI prototype to the SGP CART CF, near Billings, Oklahoma. During the period March 1993 through March 1994, the AERI prototype was operated manually by site operators only during intensive observation periods (IOPs) until proper facilities could be made ready at the site to allow more continuous operation. In December 1993, the AERI prototype began operation from the CART CF optical trailer through an open hole in the trailer ceiling. Beginning with the Remote Cloud Sensing IOP in April 1994, the operational configuration of the AERI prototype in the SGP CART CF remained stable until its replacement (the AERI-01) arrived on site in April 1995. Milestones in the AERI prototype operations from the ARM SGP CART CF are given in Table 1.1. A picture of the prototype instrument installed in the CART CF optical trailer is shown in Figure 1.1. Note especially the chimney-like tube connecting the AERI prototype to an automated hatch over the open hole in the trailer ceiling. The operational configuration of the AERI-01 facility instrument was designed to avoid the need for a similar chimney by protruding out the side of the trailer.

Table 1.1. Milestones in the AERI Prototype Operations from the ARM SGP CART CF

Date	Milestone
15 March 1993	Deployment of AERI prototype to SGP CART CF
August 1993	AERI prototype moved to Optical Trailer
December 1993	Automated hatch with chimney installed in optical trailer Begin routine operations from optical trailer
11 April 1994	AERI prototype setup modified slightly
25 April 1995	AERI-01 system arrives on site
28 April 1995	Obstruction in sky field of view (FOV) removed
31 May 1995	Real-time software modified to include hot blackbody (HBB) refinement
25 July 1995	Final day of AERI prototype data from SGP CART
26 July 1995	AERI prototype removed from SGP CART CF

1.2 Corrections

Beginning April 26, 1995, the two UW spectral radiometers (the AERI prototype and the AERI-01) operated simultaneously from the SGP CART CF optical trailer until the removal of the AERI prototype on July 26, 1995. During the early part of this period of instrument intercomparison it was realized that the AERI prototype instrument sky field of view (FOV) contained a "warm" obstruction, which partially

blocked the vertical view of the sky. Using coincident measurements of the sky from the (unobstructed) AERI-01, a radiometric correction for the FOV obstruction has been developed (by the UW) for application to AERI prototype data. In addition, some small calibration refinements to the AERI prototype data [referred to as the hot blackbody (HBB) correction] have been included in this algorithm in order to bring the data quality up to the level of the AERI-01 system. The corrected AERI prototype data is referred to as AERI-00 data to indicate a level of data quality on a par with the AERI-01 facility instrument. The obstruction in the AERI prototype sky FOV was physically removed on April 28, 1995. Details of the AERI prototype data correction algorithm (HBB and FOV obstruction) are given in Sections 2 and 3, respectively.

1.3 Examples

The AERI instrument measures the downwelling infrared spectral radiance emitted by the atmosphere in the range 3.3 - 19 μm (520 - 3000 cm^{-1}) with a spectral resolution of 0.5 cm^{-1} (unapodized). This spectral region is split into two data channels (ch1: 520-1800 cm^{-1} and ch2: 1800-3000 cm^{-1}) for signal to noise optimization. A 3.5-minute sky dwell is obtained every 10 minutes with views of high emissivity HBB and ambient blackbody (ABB) cavities interspersed between each sky view.

A typical AERI measurement of a relatively dry clear atmosphere is shown in Figures 1.2 and 1.3 for channels 1 (longwave) and 2 (shortwave), respectively. Also shown (on an expanded scale) are the spectral shape, sign, and magnitude of the corrections applied to the AERI prototype data. As these figures indicate, the sign of the calibration correction for the HBB and the FOV obstruction corrections are opposite and these corrections partially cancel one another. However, the magnitude of the FOV obstruction is substantially greater than the HBB correction and is the dominant effect in the total correction shown. Figures 1.4 and 1.5 illustrate the same correction for a considerably moister atmospheric condition, as evidenced by the relatively larger radiance in the infrared window region (800-1200 cm^{-1}). As indicated in these figures, the size of the correction is smaller (in both absolute and relative terms) for the clear wet (or cloudy) atmosphere than for the clear dry atmosphere. This is because the FOV obstruction correction is proportional to the difference between the sky window radiance and the temperature (near ambient) of the obstruction itself.

Error estimates of this correction can be found in Section 3 on the FOV correction. Comparison of coincident AERI-00 data and AERI-01 data are also presented in Section 4.

1.4 Correction Implementation

The corrections discussed above have been implemented at the UW as an Interactive Data Language (IDL) procedure. The correction script, referred to as "aeri00corr.pro" version 1.6 (August 10, 1995), is given in Section 5. The algorithm has also been implemented (by Dave Turner) as a c-language procedure at the ARM Experiment Center. The Experiment Center, using a routine, which corrects for both the sky FOV obstruction and the HBB temperature and emissivity, reprocessed the AERI prototype data from April 11, 1994, through April 28, 1995.

The data beginning April 29, 1995, after the obstruction was physically removed, requires only the small correction for the HBB temperature and emissivity. The Experiment Center also reprocessed this data from April 29 through May 31, 1995, using a subset of the algorithm given in Section 5.

On May 31, 1995, the AERI real-time software was modified to include the HBB correction; thus no correction is needed to the AERI prototype data from June 1 through the last day (July 25, 1995) that the AERI prototype data was obtained by the ARM data system. The ARM Experiment Center has also reprocessed the AERI prototype data from this period (although no radiance corrections were required) in order to include certain value added products and to create a consistent data set. The entire reprocessed AERI data set (April 1994 through July 1995) is available from the ARM Experiment Center upon request.

The AERI prototype data from March 15, 1993, through April 10, 1994, have not yet been corrected. The removal of any sky FOV obstruction is complicated by the lack of any coincident spectral observations during this period. The best approach to be used in correction of this data is under study; meanwhile these data should be used with caution. Further details are available by contacting Bob Knuteson at UW-Madison.

Additional information is available on the following topics:

- HBB correction details (Section 2)
- FOV correction details (Section 3)
- AERI-00 and AERI-01 intercomparisons (Section 4)
- IDL correction script (Section 5).



Figure 1.1. The AERI prototype as it was configured inside the SGP CART CF optical trailer near Billings, Oklahoma. The white box and the black chimney-like structure acts to insulate the AERI scene mirror and blackbodies from the ambient room air while providing a vertical view of the sky through a ceiling hatch. The edge of the viewing hole in the white box was responsible for the obstruction in the sky FOV.

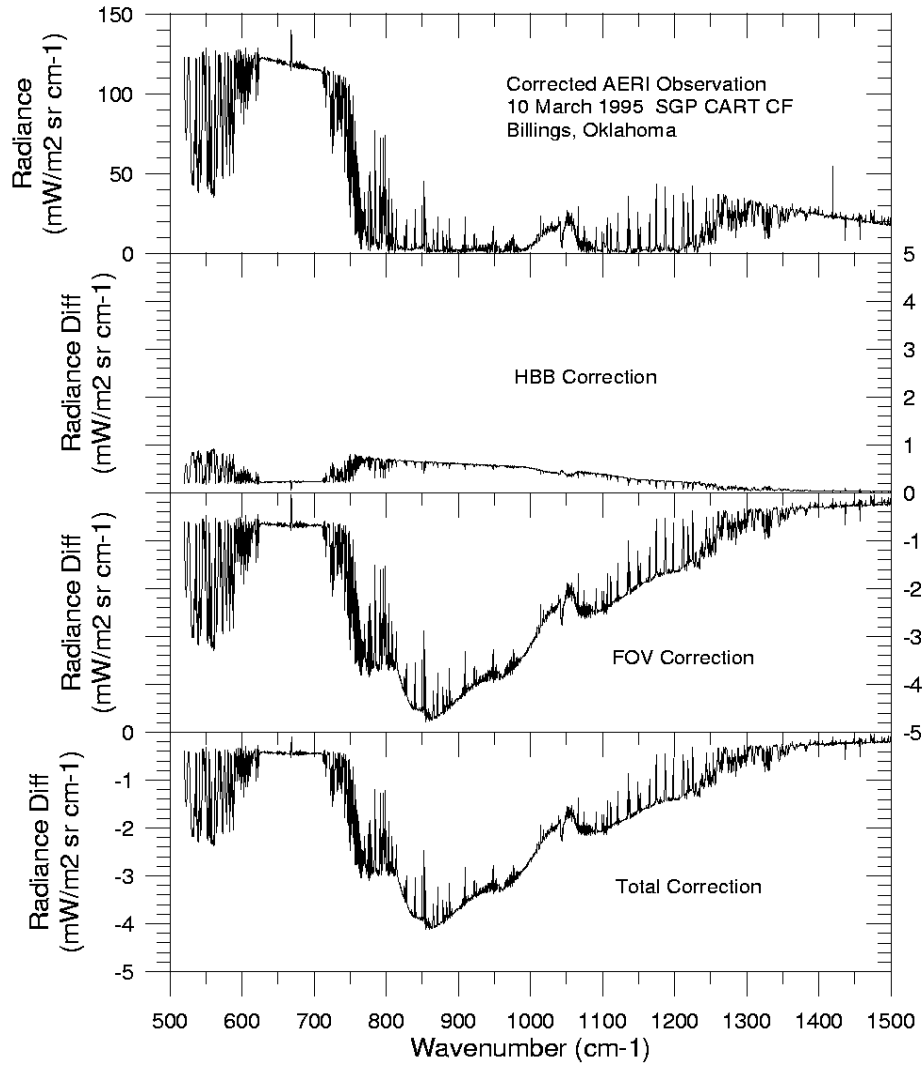


Figure 1.2. Example of a corrected AERI observation (channel 1) for a clear, dry atmosphere (March 10, 1995, 05:30 Universal Time Coordinate (UTC), SGP CART site near Billings, Oklahoma). The upper panel contains the corrected AERI observation. The second panel from the top contains the HBB correction spectrum. The third panel contains the FOV correction spectrum. The bottom panel contains the total correction, which incorporates both of the previous two corrections.

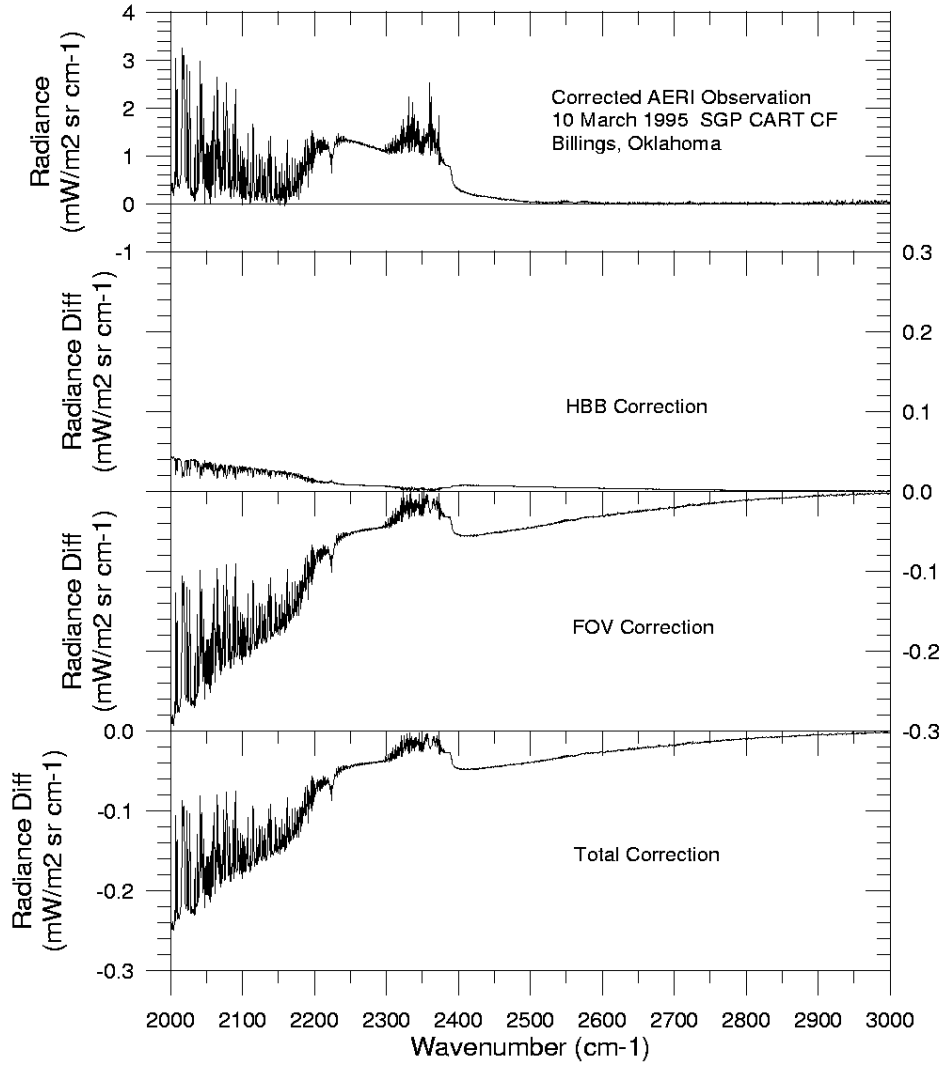


Figure 1.3. Example of a corrected AERI observation (channel 2) for a clear, dry atmosphere (March 10,1995, 05:30 UTC, SGP CART site near Billings, Oklahoma). The upper panel contains the corrected AERI observation. The second panel from the top contains the HBB correction spectrum. The third panel contains the FOV correction spectrum. The bottom panel contains the total correction, which incorporates both of the previous two corrections.

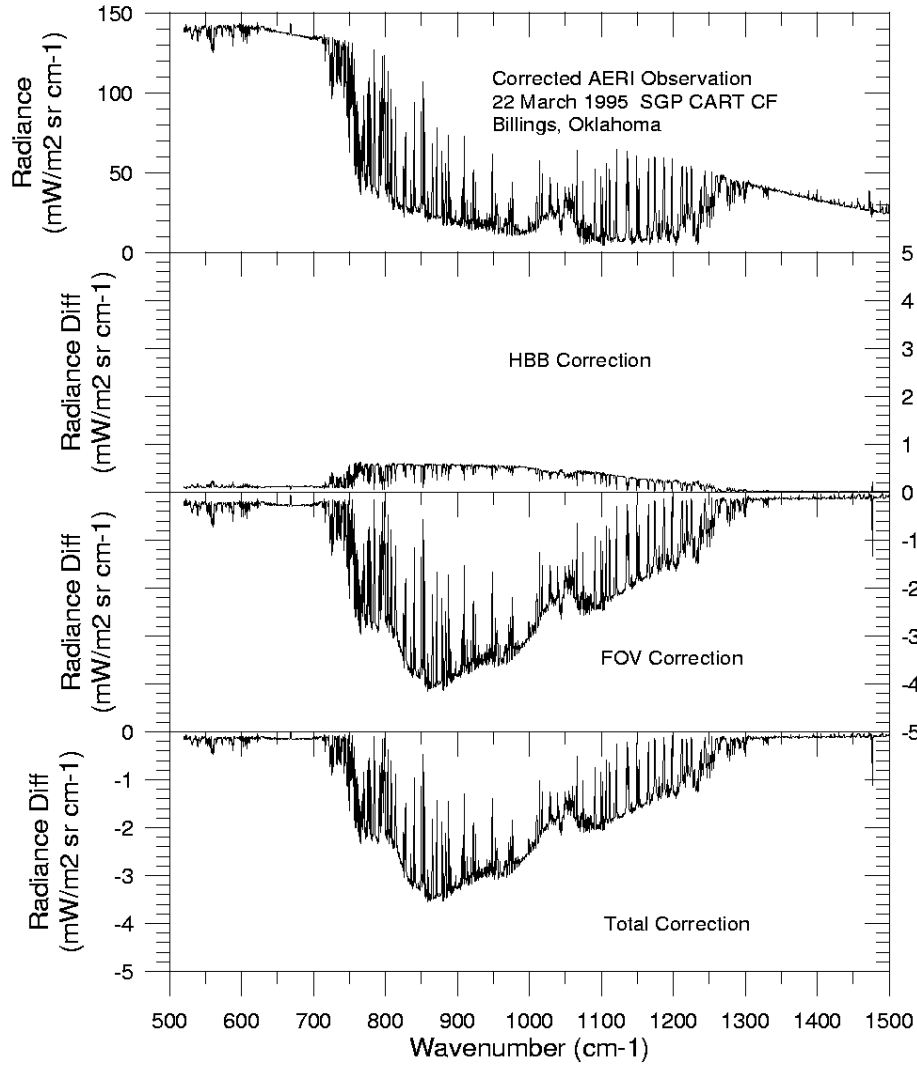


Figure 1.4. Example of a corrected AERI observation (channel 1) for a clear, moist atmosphere (March 22, 1995, 05:30 UTC, SGP CART site near Billings, Oklahoma). The upper panel contains the corrected AERI observation. The second panel from the top contains the HBB correction spectrum. The third panel contains the FOV correction spectrum. The bottom panel contains the total correction, which incorporates both of the previous two corrections.

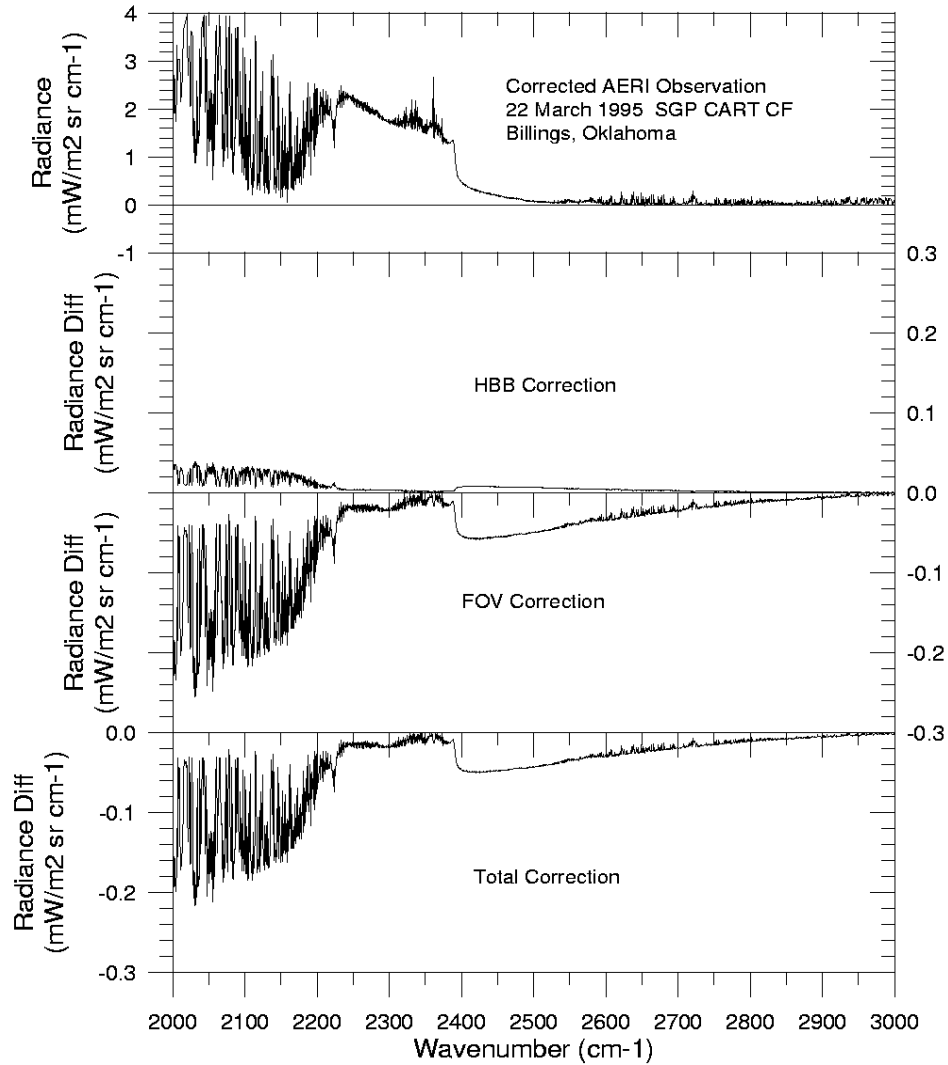


Figure 1.5. Example of a corrected AERI observation (channel 2) for a clear, moist atmosphere (March 22, 1995, 05:30 UTC, SGP CART site near Billings, Oklahoma). The upper panel contains the corrected AERI observation. The second panel from the top contains the HBB correction spectrum. The third panel contains the FOV correction spectrum. The bottom panel contains the total correction, which incorporates both of the previous two corrections.

2. Hot Blackbody Cavity Correction

In order to understand the HBB cavity correction, it is useful to review the characteristics of the blackbodies being used. Figure 2.1 shows a cross section of the blackbody cavity used in the AERI prototype. The cavity is symmetric about the central axis of the blackbody with the middle section of the body wrapped with heating coils to produce a constant input heat source. The inside of the blackbody is coated with paint (Chemglaze Z306 flat black) that is black in the visible and the infrared. Temperatures are monitored at three locations: two around the cylindrical portion of the blackbody (referred to as top and bottom), and one at the apex of the cavity cone. The radiometric calibration of the spectral sky emission requires knowledge of both the effective cavity temperature and effective cavity emissivity. The HBB correction described here simply reflects an adjustment to the effective cavity temperature and emissivity based upon a more thorough analysis of the blackbody characteristics that was conducted at the UW since the deployment of the AERI prototype system at the SGP CART site in March 1993.

The current model for the HBB effective cavity temperature is based upon weighting of the available temperature monitoring points in the form

$$T_{\text{hbb}} = W_{\text{top}} \cdot T_{\text{top}} + W_{\text{bot}} \cdot T_{\text{bot}} + W_{\text{apex}} \cdot T_{\text{apex}} \quad (2.1)$$

where T_{hbb} is the effective cavity temperature used in radiometric calibration, T_{hbb} , T_{bot} , and T_{apex} are the measured temperatures at the top, bottom, and apex monitoring points, and W_{top} , W_{bot} , and W_{apex} are the respective relative weighting factors (i.e., $W_{\text{top}} + W_{\text{bot}} + W_{\text{apex}} = 1$). The weights, W , are deduced from a geometrical analysis of the cavity, which makes use of the overlap of the actual AERI FOV as projected onto the inside cavity surface, and the linear temperature gradient, which thermal modeling indicates between the top (or bottom) monitoring point and the cone apex. Since the AERI FOV is centered along the axis of the blackbody and assuming thermal symmetry about the axis, the top and bottom weights must be equal (i.e., $W_{\text{top}} = W_{\text{bot}}$). The relative weighting of the apex compared to the top (or bottom) monitoring points is obtained by equal weighting of the emitting area for each field angle of the AERI FOV. This is an approximation, which ignores the reflected contribution from the rest of the cavity. It is sufficiently valid because of the small thermal gradient in the cavity and the high paint emissivity. Given the size of the AERI prototype blackbodies and the AERI prototype FOV diameter at the entrance to the blackbodies one obtains the following weights: $W_{\text{top}} = W_{\text{bot}} = 0.107$, $W_{\text{apex}} = 0.786$. The temperatures, T , in Eq. (2.1) are intended to represent measured temperatures at the top, bottom, and apex of the blackbody cavity obtained at the time of the HBB view. Unfortunately, the apex temperature was not recorded in the AERI prototype data stream (unlike the final AERI system where all three temperatures are recorded simultaneously). However, the gradient between top (or bottom) and the apex was measured in the lab under conditions consistent with the operating environment at the SGP CART CF. Note that one side effect of the AERI prototype set up inside the optical trailer was that the ambient air temperature surrounding the HBB was maintained within a few degrees of 20 °C at all times. Therefore the HBB gradient measured in the lab has been used as an offset to the temperature that was previously used in the calibration (T_{top}) to obtain an estimate of T_{apex} (i.e., $T_{\text{apex}} = T_{\text{top}} - \text{Gradient}$). The temperature gradient used

in the correction was 0.24 °C. Taking the relative weights into account, the actual effective temperature correction made to the AERI prototype HBB temperature is $T_{\text{new}} = T_{\text{original}} - \text{Gradient} \cdot W_{\text{apex}} = T_{\text{original}} - 0.1886 \text{ °C}$.

The effective cavity emissivity is obtained from a measurement of the paint emissivity on a flat surface and a calculation that accounts for the multiple internal reflections inherent in the cavity design. The paint emissivity was obtained from several witness samples of the paint applied to flat squares of aluminum at the same time that the cavity blackbodies were painted. These witness samples were sent to Labsphere, Inc., North Sutton, New Hampshire, who obtained the results represented in Figure 2.2. It is believed that the main spectral variation of the emissivity is due to a contribution of the undercoat seen through the black overcoat. The earlier estimate of emissivity used a constant value in each AERI channel ($p_v = 0.946$ in channel 1, [500, 1800 cm^{-1}], and $p_v = 0.921$ in channel 2, [1800, 3000 cm^{-1}]) chosen to match the paint emissivity in the atmospheric window regions where the effect on AERI calibration is greatest. The revised emissivity estimate is shown as a smooth fit to the measured paint emissivity and now includes the spectral dependence of the emissivity.

Given the paint emissivity, p_v , the cavity emissivity, e_v , is given by

$$e_v = \frac{p_v}{p_v + f(1 - p_v)} \quad (2.2)$$

where $C_f = 1/f$ is the cavity factor. Using the Jet Propulsion Laboratory Tech Report No. 32-1463 (C.L. Sydnor) the cavity factor computed for the AERI blackbody is 12.79. The earlier estimate of paint emissivity led to the use of the following constant cavity emissivities; $e_v = 0.9956$ in channel 1, and $e_v = 0.9933$ in channel 2. Use of the spectrally dependent emissivity shown in Figure 2.2 makes small but important improvements to the calibrated radiance over the earlier use of a constant emissivity in each AERI channel.

The procedure used to correct the calibrated AERI prototype radiance to account for a change in the HBB effective temperature and emissivity uses the calibration equation

$$N_v = Q_v * [B_v(T_{\text{hbb}}) - B_v(T_{\text{abb}})] + B_v(T_{\text{abb}}) \quad (2.3)$$

rewritten in the form

$$Q_v = \frac{[N_v - B_v(T_{\text{abb}})]}{[B_v(T_{\text{hbb}}) - B_v(T_{\text{abb}})]} \quad (2.4)$$

where N_v is the calibrated sky radiance, $B_v(T)$ is the effective Planck radiance $P_v(T)$ including the emissivity e_v and corresponding reflected temperature T_{refl} ,

$$B_v(T) = e_v \cdot P_v(T) + (1 - e_v) \cdot P_v(T_{\text{refl}}) \quad (2.5)$$

and Q_v is the real part of the complex counts ratio

$$Q_v = \text{Re} \left\{ \frac{C_v^{\text{sky}} - C_v^{\text{abb}}}{C_v^{\text{hbb}} - C_v^{\text{abb}}} \right\}. \quad (2.6)$$

The correction procedure is to compute Eq. (2.4) with the original effective temperature and emissivity to obtain the ratio Q_v , then apply Eq. (2.3) with the new corrected effective temperature and emissivity to obtain the final corrected spectrum. This procedure avoids having to compute Q_v from Eq. (2.6), a computationally onerous task. Instead the correction requires only information already available in the AERI radiance data stream.

The HBB correction was validated using data from May 2, 1995, after the obstruction in the AERI prototype had been physically removed, when the AERI prototype and the final AERI system (AERI-01) were operating simultaneously at the SGP CART site.

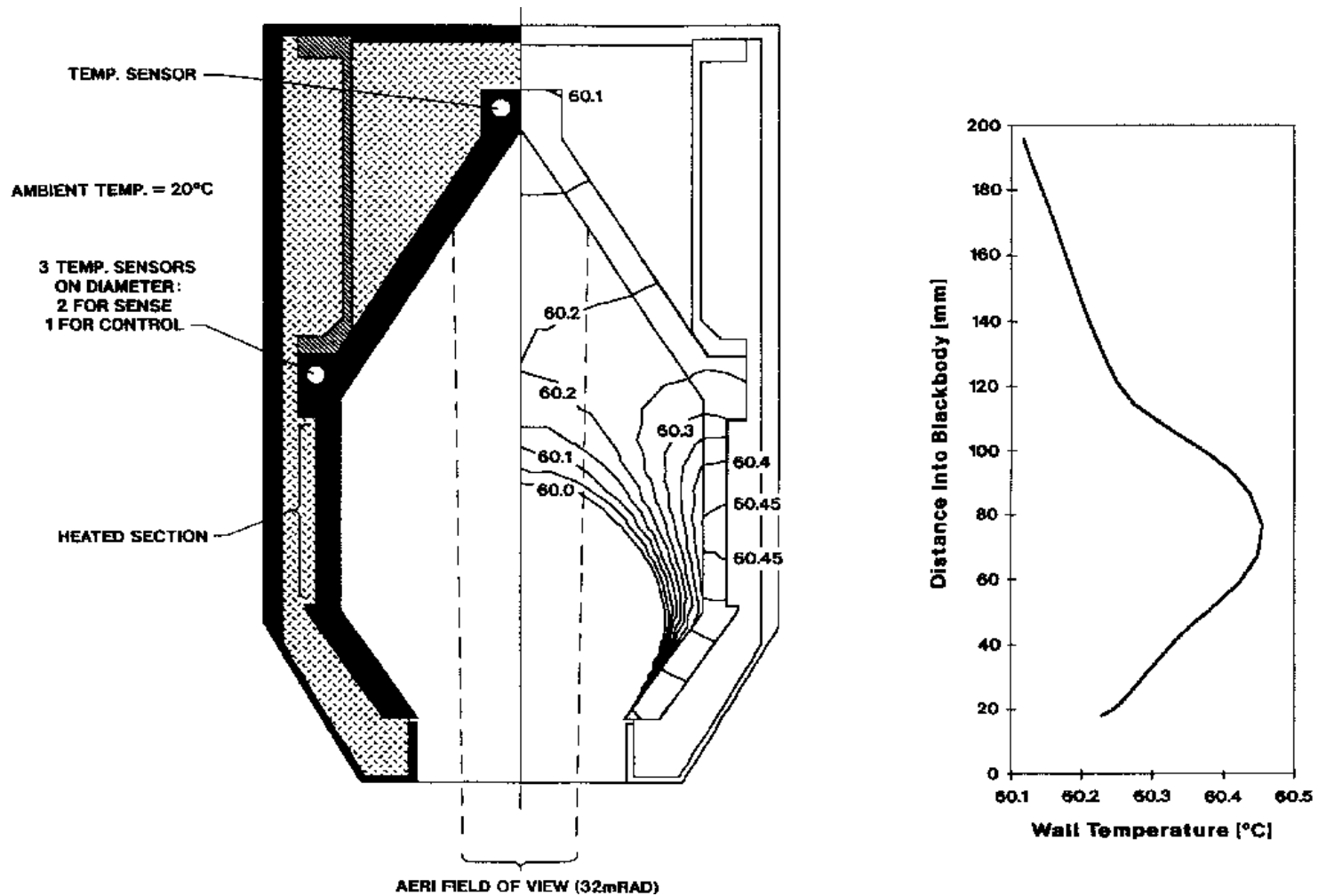


Figure 2.1. AERI blackbody cavity cross section. The AERI blackbodies used for radiometric calibration were designed and built at the UW - Madison Space Science and Engineering Center. The temperature profiles shown in this figure are from a thermal model of the cavity operating at 60 °C above ambient.

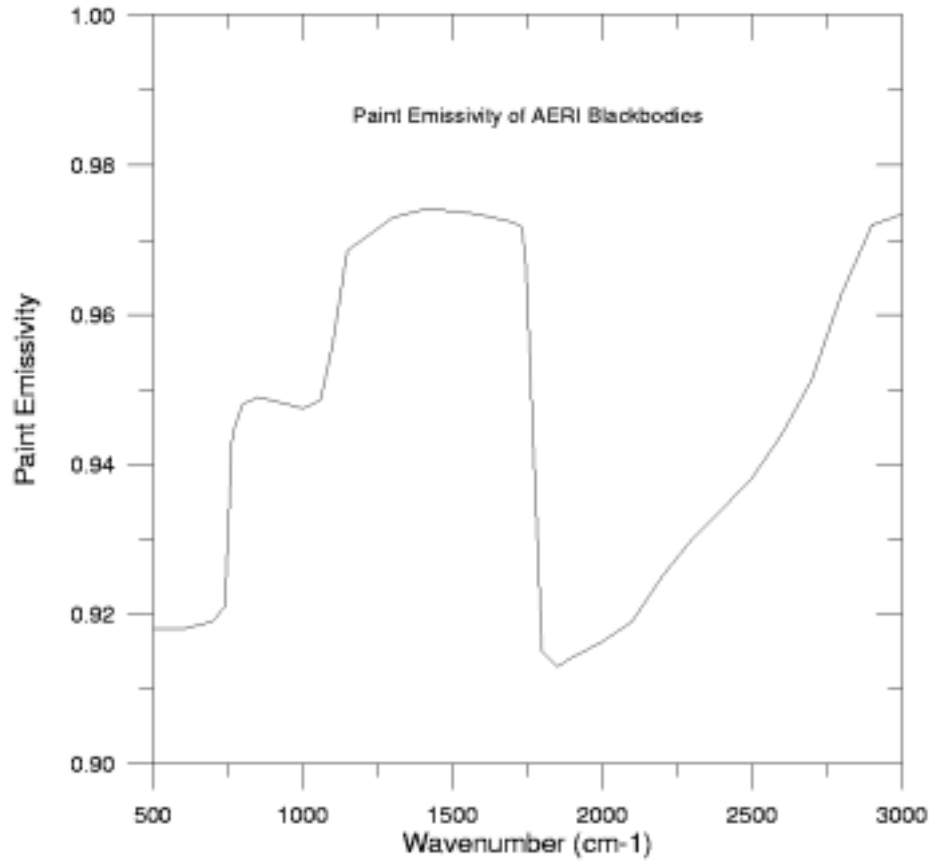


Figure 2.2. Paint emissivity used in AERI blackbodies. This curve is a representation of the paint emissivity derived from spectral scans of witness samples by Labsphere, Inc. The stated uncertainty is 2%. Note that the cavity effect makes the blackbody effective emissivity greater than 0.993 for all wavelengths.

3. Sky Field of View Obstruction Correction

The nominal setup for the AERI prototype instrument (hereafter, AERIPROTO) at the ARM site had it encased in a white-painted plywood and styrofoam box which was connected to the roof opening with a circular tube (chimney), as shown in Figure 1.1. A circular hole in the plywood box allowed unobstructed sky viewing. Examination of the setup in April 1995 found the plywood box misaligned with the AERIPROTO sky view, causing part of the box to be in the FOV. This small area blocked part of the incoming sky radiation while emitting Planck radiation of its own. A more detailed investigation finds that the box edge also scattered sky+chimney radiation into the beam at near grazing angle, as described in Section 3.1. If the true sky radiance is $N_{\text{sky},v}$, the AERIPROTO instrument measured the radiance N_v given by (Eq. [3.11] from Section 3.1)

$$N_v = (1 - \tilde{f}_v) N_{\text{sky},v} + \tilde{f}_v B_v(T_{\text{eff}}) \quad (3.1)$$

where \tilde{f}_v is the effective obstruction area, normalized to the total viewing area of the instrument, and T_{eff} is the effective box temperature. Both of these quantities are derived in Section 3.1. The effective obstruction area has a wavelength dependence because it varies with the box emissivity.

The effective obstruction area can be calculated from sky measurements obtained when both the AERIPROTO and AERI-01 instruments operated simultaneously on April 26, 1995: AERI-01 provided a measurement of $N_{\text{sky},v}$, and AERIPROTO measured N_v . The effective temperature of the obstruction is estimated to be halfway between the temperatures measured at the instrument and the top of the chimney. Errors associated with this temperature are described in Section 3.2. With these known quantities, \tilde{f}_v is calculated from rearrangement of Eq. (3.11) (Eq. [3.14])

$$\tilde{f}_v = \left[\frac{N_v - N_{\text{sky},v}}{B_v(T_{\text{eff}}) - N_{\text{sky},v}} \right]_{950426} = \left[\frac{N_{\text{AERIPROTO}} - N_{\text{AERI01},v}}{B_v(T_{\text{eff}}) - N_{\text{AERI01},v}} \right]_{950426} \quad (3.2)$$

This quantity is stable in time since the box was not moved during the entire time in which it partially obstructed the AERIPROTO sky view. After calculating \tilde{f}_v , the true sky radiance can be estimated for any measurement obtained during this time period as (Eq. [3.15])

$$N_{\text{sky},v} = \frac{N_v - \tilde{f}_v B_v(T_{\text{eff}})}{1 - \tilde{f}_v} \quad (3.3)$$

Some sample correction spectra are shown later in Figure 3.7 with estimated errors in Figure 3.8. The maximum obstruction correction was 4 mW/m²/cm⁻¹/sr in channel 1 (the longwave channel, top in Figures 3.1 through 3.8), and 0.3 mW/m²/cm⁻¹/sr in channel 2 (the shortwave channel, bottom in

Figures 3.1 through 3.8). The errors are conservatively estimated at $<0.5 \text{ mW/m}^2/\text{cm}^{-1}/\text{sr}$ in Channel 1, and $<0.05 \text{ mW/m}^2/\text{cm}^{-1}/\text{sr}$ for wavenumbers greater than 2000 cm^{-1} . Section 3.1 derives the correction in detail and Section 3.2 estimates errors.

3.1 Correction

Figure 3.1 shows a typical clear-sky radiance spectrum from the AERIPROTO instrument. The effects of the obstruction on the radiation properties are shown in Figure 3.2, where the AERIPROTO spectrum is compared to the AERI-01 spectrum. The differences in the opaque regions are due to air temperature differences rather than the obstruction; AERI-01 was stationed outside, so the air surrounding it was at a cooler temperature than the air viewed by AERIPROTO inside the chimney.

Figure 3.3 shows a schematic diagram of the effect of the obstruction on the observed sky spectrum. Let Ω be the solid angle of sky the instrument would see if there were no obstruction. The obstruction blocks from view a solid angle area of $\Omega_1 + \Omega_2$, from the underside of the box (Ω_1) and the box edge (Ω_2). The fractional obstruction areas are $f_1 = \Omega_1/\Omega$, for the bottom of the box, and $f_2 = \Omega_2/\Omega$ for the side.

The obstruction emits Planck radiation and scatters radiation in accordance with its emissivity characteristics: The intensity per unit wavenumber, R_v , of radiation from the box is given by

$$R_v = \epsilon_v B_v(T) + (1 - \epsilon_v) A_v \quad (3.4)$$

where A_v is the radiation incident on the surface and ϵ_v is the emissivity. We will divide the radiation R_v into two parts, due to the bottom and side. The underside of the box both emits and reflects Planck radiation, since it does not see sky radiation. The Planck radiation reflected from the underside of the box should have a temperature close to that of the box, so Eq. (3.4) can be written

$$\begin{aligned} R_{v,1} &= \epsilon_{v,1} B_v(T_{\text{box}}) + (1 - \epsilon_{v,1}) B_v(T_{\text{ref}}); \\ &\approx B_v(T_{\text{box}}) \end{aligned} \quad (3.5)$$

that is, the effective emissivity is equal to 1. The side of the box emits Planck radiation, and scatters into the AERIPROTO view a mixture of sky radiation and possibly Planck radiation from the surface of the chimney, all at a near-grazing angle:

$$R_{v,2} = \epsilon_v B_v(T_{\text{box}}) + a(1 - \epsilon_v) N_{\text{sky},v} + (1 - a)(1 - \epsilon_v) B_v(T_{\text{chimney}}), \quad (3.6)$$

where ϵ_v is the emissivity of the side of the box, and a is the fraction of scattered light that is due to sky radiation.

The contributions to the measured AERIPROTO radiance, N_v , are

$$N_v = (1 - f_1 - f_2) N_{\text{sky},v} + f_1 R_{v,1} + f_2 R_{v,2}. \quad (3.7)$$

The first term of the right-hand side is unobstructed sky radiance reaching the instrument; and the last two terms are the components from the underside and side of the box (Figure 3.3). Substituting Eqs. (3.5) and (3.6) into (3.7), and rearranging gives

$$N_v = (1 - \tilde{f}_v) N_{\text{sky},v} + f_{a,v} B_v(T_{\text{box}}) + (\tilde{f}_v - f_{a,v}) B_v(T_{\text{chimney}}), \quad (3.8)$$

where

$$f_{a,v} = (f_1 + \epsilon_v f_2) \quad (3.9)$$

and

$$\tilde{f}_v = (f_1 + f_2 - f_2 a (1 - \epsilon_v)). \quad (3.10)$$

The values of f_1 , f_2 , a , and ϵ_v are not known separately. However, if we define a new temperature as a weighted mean between T_{box} and T_{chimney} , Eq. (3.8) simplifies to:

$$N_v = (1 - \tilde{f}_v) N_{\text{sky},v} + \tilde{f}_v B_v(T_{\text{eff}}) \quad (3.11)$$

if

$$B_v(T_{\text{eff}}) = w B_v(T_{\text{box}}) + (1 - w) B_v(T_{\text{chimney}}) \quad (3.12)$$

where

$$w = f_{a,v} / \tilde{f}_v. \quad (3.13)$$

The form of Eq. (3.11) is no more complicated than the simple case in which the obstruction emits Planck radiation with no scattered component; in that case, the emissivity ϵ_v is equal to 1, and it follows that $w = 1$, $T_{\text{eff}} = T_{\text{box}}$, and $\tilde{f}_v = f_1 + f_2$ is just the geometric obstruction area. We will show later (Section 3.2) that the exact value of the temperature weighting only weakly affects the size of the correction. We can think of the term \tilde{f}_v as the effective obstruction area, which varies with wavenumber if the emissivity varies.

Using Eq. (3.11) to describe the AERIPROTO measured radiance allows a way to calculate the obstruction effect if N_{sky} is known. On April 26, 1995, with both instruments operating simultaneously, the AERI-01 spectrum provided us with N_{sky} , and we can solve for \tilde{f}_v using Eq. (3.11):

$$\tilde{f}_v = \left[\frac{N_v - N_{\text{sky},v}}{B_v(T_{\text{eff}}) - N_{\text{sky},v}} \right]_{950426} = \left[\frac{N_{\text{AERIPROTO}} - N_{\text{AERI01},v}}{B_v(T_{\text{eff}}) - N_{\text{AERI01},v}} \right]_{950426} \quad (3.14)$$

The only unknown left in this equation is the effective box temperature. We choose this to lie halfway between the ambient blackbody measured at the AERIPROTO instrument, and the outside temperature measured at the top of the chimney, since the box lies between these positions. Both of these temperatures are recorded in the AERIPROTO data file header.

During three clear and stable time periods on April 26, 1995, we calculated \tilde{f}_v using Eq. (3.14) and derived the same fit for all three cases. This function is shown in Figure 3.4 for the two AERI data channels. Note that channel 1, the longwave channel (top of Figure 3.4), has variable emissivity. The shortwave function (bottom, Figure 3.4) has more variations than we choose to fit, because they do not appear to be due solely to the obstruction. As Figure 3.4 shows, the evaluation of \tilde{f}_v becomes inaccurate in the opaque channels because the two instruments saw different nearby-air temperatures, with AERIPROTO viewing about 2 meters of heated air inside the optics trailer; in effect, the substitution of AERI-01 radiance for N_{sky} is inaccurate in the opaque region. The fit to \tilde{f}_v in these regions is therefore an extrapolation from the window region. Fortunately, the obstruction effect is smallest in the opaque region, as shown below, so this uncertainty should be relatively unimportant.

The effective obstruction area calculated from Eq. (3.14) depends on the true obstruction area, the emissivity of the box, and the fraction of scattered radiation due to sky versus chimney. As long as the AERIPROTO and box remained in the same configuration, this quantity should be time independent. Therefore, after solving for it using the data from April 26, 1995, \tilde{f}_v can be considered a known quantity and substituted into Eq. (3.11) to solve for the true sky radiance observed at all times during the period that the obstruction was in this configuration:

$$N_{\text{sky},v} = \frac{N_v - \tilde{f}_v B_v(T_{\text{eff}})}{1 - \tilde{f}_v} \quad (3.15)$$

As a first check, application of Eq. (3.15) to the April 26, 1995, AERIPROTO data compared to the AERI-01 data is shown in Figure 3.5. The channel 1 differences are zero within the noise, except in the opaque regions, where the warmer path through the chimney for the AERIPROTO becomes apparent compared to the AERI-01 instrument which sits outside. The channel 2 differences are less well behaved. However, a comparison of the two instruments after the obstruction was physically removed (Figure 3.6), shows similar features in the window regions, so the cause is probably due to something other than the obstruction. In the example shown in Figure 3.6 the date of observation was May 2, 1995, and both instruments were outside, so the opaque regions agree better.

Rewriting Eq. (3.11) provides another way to view the correction:

$$\text{CORR} = N_v - N_{\text{sky},v} = \frac{\tilde{f}_v (B_v(T_{\text{eff}}) - N_v)}{1 - \tilde{f}_v}. \quad (3.16)$$

This calculation shows that the correction is greatest where the sky radiation deviates most from the Planck radiation of the box; this would be in the window region. In the opaque region of the spectrum, the instrument sees a blackbody at the local air temperature, which should be close to that of the plywood box. The correction should be a small offset corresponding to the difference between Planck radiation at two nearby temperatures. As Figure 3.7 shows, the correction is greatest in the window region for clear scenes where the difference between the sky radiation (at the coldest temperatures) and the ambient blackbody radiation is greatest (see Figure 3.2 for comparison to the radiance spectra). Figure 3.7 shows the correction under various clear-sky meteorological conditions. The peak correction magnitude is about 4 mW/m²/cm⁻¹/sr in channel 1, and 0.3 mW/m²/cm⁻¹/sr in channel 2. Under cloudy skies, the correction will be smaller than this, because N_v is closer to $B_v(T_{\text{eff}})$ than in the clear-sky case (Eq. [3.16]).

3.2 Errors

The error in the correction is reasonably small, less than 10% of the correction itself. The greatest source of error in the obstruction correction is probably the uncertainty in our knowledge of the effective box temperature, T_{eff} . This leads to uncertainty in the derivation of the effective obstruction area. For example, if our guess was a few degrees warmer than the true temperature, we have overestimated the amount of radiation from the box, $B_v(T_{\text{eff}})$, and therefore underestimated the effective obstruction area determined from our simultaneous observations with AERIPROTO and AERI-01 (using Eq. [3.14]). When we apply the correction on a given date, using Eq. (3.15) or (3.16), we have the added uncertainty in the knowledge of T_{eff} affecting our estimate of $B_v(T_{\text{eff}})$ at the time of the observation. The change in sky radiance due to these uncertainties is

$$\Delta N_{\text{sky},v} \cong \frac{\partial N_{\text{sky},v}}{\partial \tilde{f}_v} \Delta \tilde{f}_v + \frac{\partial N_{\text{sky},v}}{\partial T_{\text{eff}}} \Delta T_{\text{eff}} . \quad (3.17)$$

Taking the derivatives (Eq. [3.15]) gives

$$\Delta N_{\text{sky},v} \cong \frac{N_v - B_v}{(1 - \tilde{f}_v)^2} \Delta \tilde{f}_v - \frac{\tilde{f}_v}{1 - \tilde{f}_v} \frac{\partial B_v}{\partial T_{\text{eff}}} \Delta T_{\text{eff}} \quad (3.18)$$

Now we can write the uncertainty in \tilde{f}_v due to that in obstruction temperature on the day in which the fit was calculated, April 26, 1995, as

$$\Delta \tilde{f}_v \cong \left[\frac{\partial \tilde{f}_v}{\partial T_{\text{eff}}} \Delta T_{\text{eff}} \right]_{950426} . \quad (3.19)$$

Taking the derivative of \tilde{f}_v (Eq. 3.14) and rearranging terms gives

$$\Delta\tilde{f}_v \cong \frac{\tilde{f}_v(1-\tilde{f}_v)}{(N_v - B_v)_{950426}} \frac{\partial B_v}{\partial T_{\text{eff}}} (\Delta T_{\text{eff}})_{950426}. \quad (3.20)$$

Substituting this into Eq. (3.18) gives

$$\Delta N_{\text{sky},v} \cong \frac{\tilde{f}_v}{1-\tilde{f}_v} \frac{\partial B_v}{\partial T_{\text{eff}}} \left[\frac{N_v - B_v}{(N_v - B_v)_{950426}} (\Delta T_{\text{eff}})_{950426} - \Delta T_{\text{eff}} \right]. \quad (3.21)$$

The remaining item to estimate is ΔT_{eff} . Since the box is located between the instrument and the top of the chimney, the effective box temperature likely lies between the temperatures measured at these positions: T_{ABB} is the temperature of the ambient blackbody measured at the instrument, and T_{outside} is the temperature measured at the top of the chimney. An estimate of the temperature is

$$T_{\text{eff}} = xT_{\text{ABB}} + (1-x)T_{\text{outside}} \pm y(T_{\text{ABB}} - T_{\text{outside}}) \quad (3.22)$$

The variable x is a weighting factor, chosen to be 0.5. While the box is located physically closer to the cold blackbody, the effective temperature is weighted by some unknown value towards the top of the chimney, as described in Section 3.1. The variable y allows for the random variation of the temperature, assuming that the weighting is not exactly constant with time. Thus the error in temperature is

$$\Delta T_{\text{eff}} \cong \frac{\partial T_{\text{eff}}}{\partial x} \Delta x + \frac{\partial T_{\text{eff}}}{\partial y} \Delta y = (T_{\text{ABB}} - T_{\text{outside}}) (\Delta x \pm \Delta y) \quad (3.23)$$

Substituting from Eq. (3.23) into Eq. (3.21) gives

$$\Delta N_{\text{sky}} \cong \text{ERR1} + \text{ERR2}, \quad (3.24)$$

where

$$\text{ERR1} = \frac{\tilde{f}_v}{1-\tilde{f}_v} \frac{\partial B_v}{\partial T_{\text{eff}}} \Delta x \left[\frac{N_v - B_v}{(N_v - B_v)_{950426}} (T_{\text{ABB}} - T_{\text{outside}})_{950426} - (T_{\text{ABB}} - T_{\text{outside}}) \right], \quad (3.25)$$

$$\text{ERR2} = \frac{\tilde{f}_v}{1-\tilde{f}_v} \frac{\partial B_v}{\partial T_{\text{eff}}} \Delta y \left[\frac{N_v - B_v}{(N_v - B_v)_{950426}} (T_{\text{ABB}} - T_{\text{outside}})_{950426} + (T_{\text{ABB}} - T_{\text{outside}}) \right], \quad (3.26)$$

and we took the absolute value of all terms containing Δy since this presumably varies randomly in time about the value zero; this will give an upper limit to the errors due to the random variations. A conservative guess for Δy is 0.2, and for Δx is 0.5. With $x = 0.5$ and $\Delta x = 0.5$, the value of $T_{\text{eff}} \pm \Delta T_{\text{eff}}$ ranges T_{ABB} to T_{outside} , which should account for all possible temperature ranges. Thus, both the ERR1 and ERR2 terms give upper limits to the error estimate.

Note that the ERR1 term (Eq. [3.25]) can be small if the conditions are similar to those on April 26, 1995, the night of the obstruction derivation, even if Δx is large, as shown in Figure 3.8. This says that an error in the choice of temperature weighting does not always lead to an error in the correction. For example, on the night for which \tilde{f}_v was derived, T_{ABB} was 298.2 and T_{outside} was 293.3. Choosing $x = 0.5$ gives an effective box temperature of 295.7. If the correct value of x is 0, then the true box temperature is 298.2, higher than estimated, meaning we underestimated $B_v(T_{\text{eff}})$, and therefore overestimated \tilde{f}_v (Eq. [3.14]). On a night with similar conditions, for example, April 25, 1994, we will again underestimate $B_v(T_{\text{eff}})$ (since we are using $x = 0.5$ instead of the correct value of $x = 0$), but since \tilde{f}_v is overestimated, the errors will cancel to some extent according to Eq. (3.15) and (3.25). On the other hand, this error can be relatively large in conditions very different from the night of derivation, if the value of x is in error. On a hot day, T_{ABB} is cooler than T_{outside} . If x should be 0 instead of 0.5, not only did we overestimate \tilde{f}_v but now we are also overestimating $B_v(T_{\text{eff}})$ and the correction (Eq. [3.16]) is larger than it should be. This error is reflected in Eq. (3.25): since $T_{\text{ABB}} - T_{\text{outside}} < 0$, the two terms add instead of partially canceling. This is illustrated in Figure 3.8. We picked the most extreme examples (dry, cool nights and hot days) to bracket the probable range of error estimates.

Based on the extreme examples shown in Figure 3.8, a conservative estimate of the errors in the obstruction correction is $<0.5 \text{ mW/m}^2/\text{cm}^{-1}/\text{sr}$ in channel 1, and $<0.05 \text{ mW/m}^2/\text{cm}^{-1}/\text{sr}$ for wavenumbers greater than 2000 cm^{-1} . Our error estimate is an upper bound to the error since the obstruction remained unchanged during the period over which the correction applies.

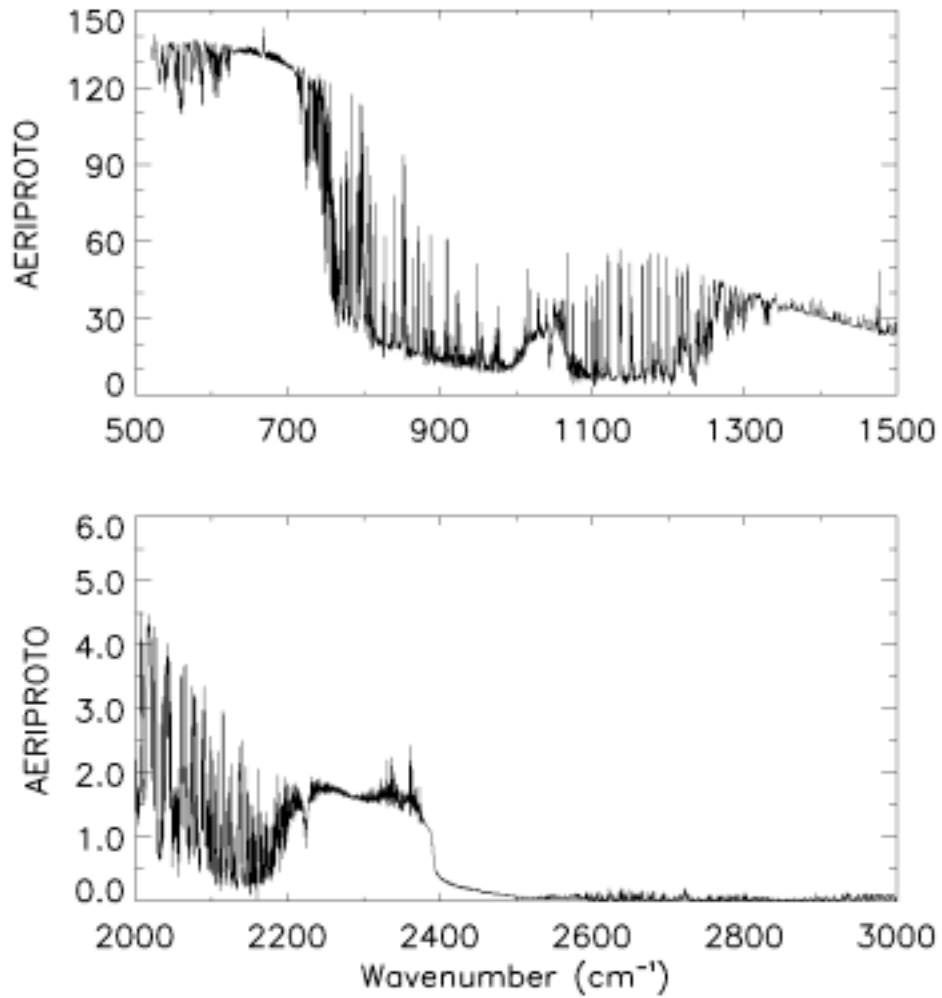


Figure 3.1. Average of 17 spectra obtained on April 26, 1995, during the time period 5.7 to 7.9 hours UTC. The radiance units here and throughout this document are $\text{mW}/\text{m}^2/\text{cm}^{-1}/\text{sr}$. The top plot is the longwave, channel 1, radiance; bottom is shortwave, channel 2.

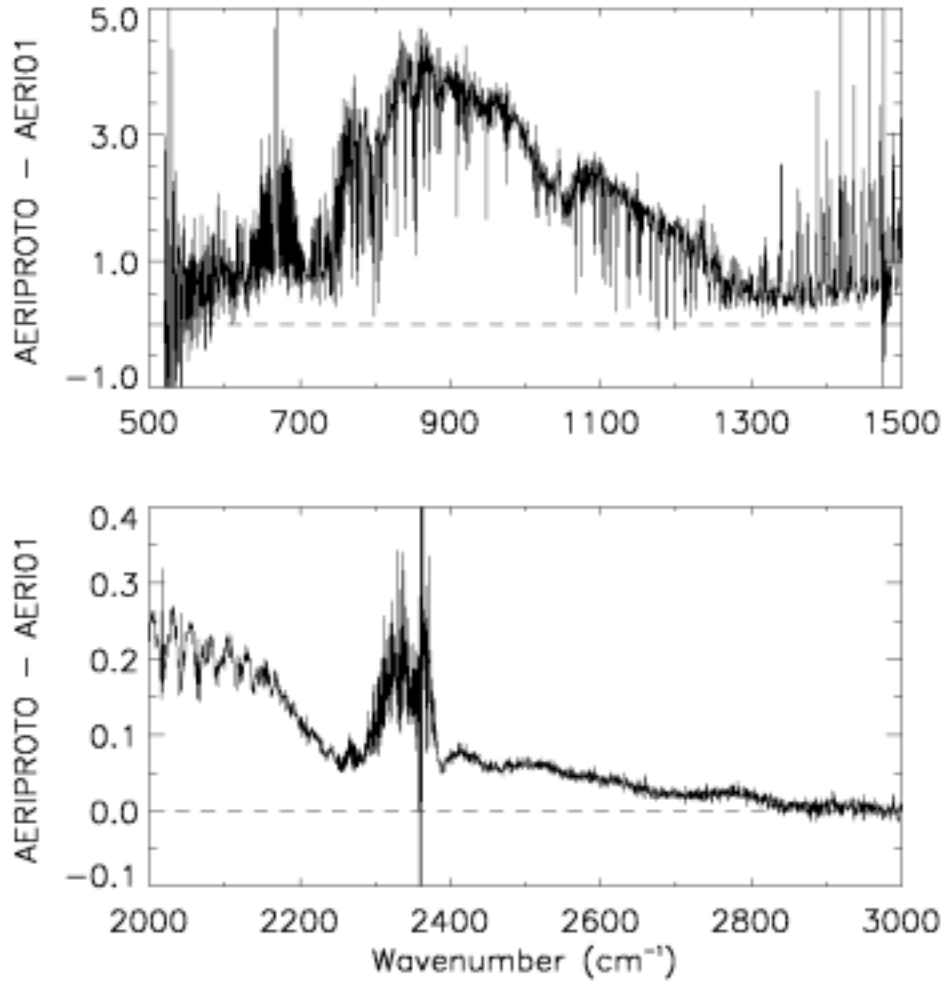


Figure 3.2. Difference spectra between the two instruments on April 26, 1995, showing the effect of the obstruction. For both instruments, 17 spectra taken during a stable clear period from 5.7 to 7.9 hours UTC are averaged. In the window regions ($750\text{--}1250\text{ cm}^{-1}$, $2000\text{--}2200\text{ cm}^{-1}$, $2400\text{--}3000\text{ cm}^{-1}$), the difference spectrum shows the radiation from the obstruction, which resembles a Planck function. The differences in the opaque regions are due to temperature differences in the nearby air surrounding the two instruments (AERIPROTO is inside a building and AERI-01 is outside), not the obstruction.

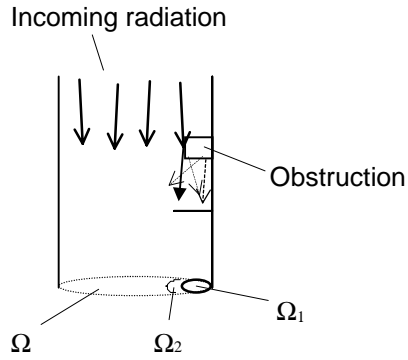


Figure 3.3. Drawing of obstruction effect in beam.

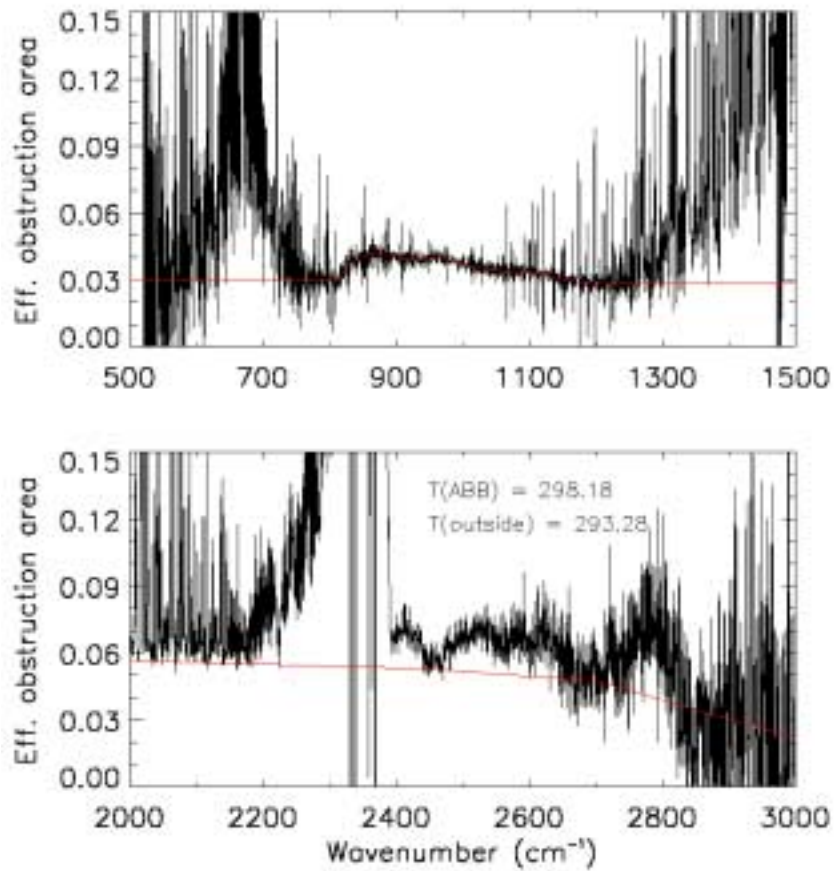


Figure 3.4. Calculation of effective obstruction area, \tilde{f}_v , using the AERIPROTO and AERI-01 spectra obtained simultaneously on April 26, 1995, and Eq. (3.14). The fit is shown as a red line. The fit in the opaque regions is an extrapolation from the window region, and is relatively unimportant since the correction is much smaller here (see text and Eq. [3.16]). The fit uses the same average of 17 spectra from the two instruments as in Figure 3.2.

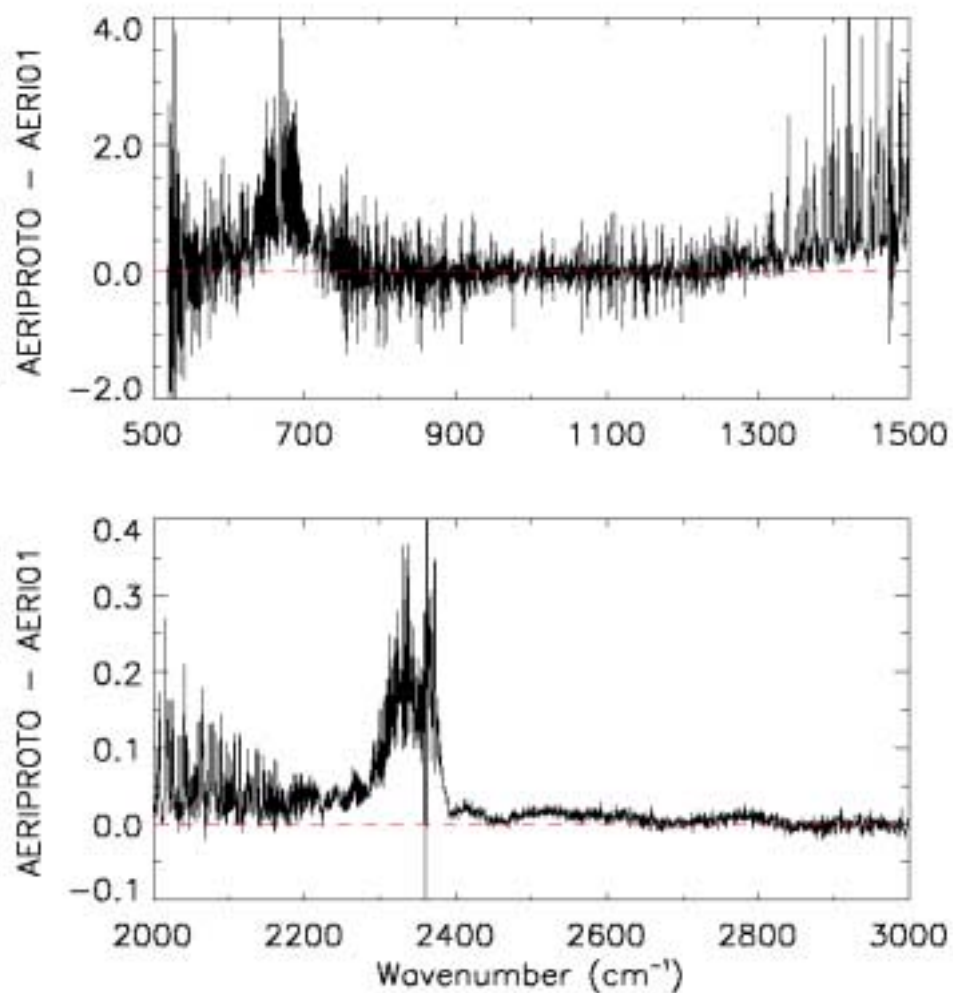


Figure 3.5. Difference spectra between the two instruments on April 26, 1995, after correcting for the obstruction, using the same data set as in Figure 3.2.

4. AERI-00 and AERI-01 Comparison

This section discusses the period of time during which two AERI instruments were operating simultaneously at the ARM SGP CART CF near Billings, Oklahoma.

The UW deployed an AERI prototype at the CART site on March 15, 1993. This system remained at the site until it was removed on July 26, 1995. Data from the AERI prototype (also referred to as the AERI-00), for the period from April 1994 through May 1995, has been reprocessed to correct for problems in the initial data processing (as discussed in an earlier section). These problems were corrected in the real-time processing beginning June 1, 1995.

On April 25, 1995, the UW deployed a second AERI system, the AERI-01, to the Oklahoma CART site as a part of the permanent installation of an AERI facility instrument in the central facility optical trailer. The period April 26 through July 6, 1995, was a checkout period for the AERI-01 system while an automated hatch was being installed to allow true continuous sky data collection. During this period a site operator manually opened the hatch over the AERI sky view. However, all changes to the initial AERI-01 real-time processing software were finalized beginning June 1, 1995.

The period June 1 through July 26, 1995, represents a unique period of instrument intercomparison from the SGP CART site. During this period, two AERI instruments (AERI-00 and AERI-01) were operating in a nearly continuous automated manner sampling essentially the same vertical sky view at nearly the same times. The AERI-00 operated from the optical trailer with the same view through the ceiling as it had since installation in the optical trailer in December 1993. The AERI-01 was also installed in the optical trailer but in its design configuration, which allows for the scene mirror and blackbodies to be outside in the ambient environment rather than inside the air-conditioned trailer as was the case for AERI-00. The other major difference in the systems was the time sampling of the sky view. The AERI-01 system sampled the sky at a somewhat faster rate (9 minutes between sky samples as opposed to 10 minutes for AERI-00). This meant that any two sky dwells (3.5 minutes in duration) could differ between the two systems by up to 5 minutes. This is not a problem for intercomparison in clear sky, but comparison of cloud radiances was influenced by the lack of time synchronization of the two systems.

An example of the comparison of the AERI-00 and AERI-01 systems during clear, nighttime conditions is shown in Figures 4.1 (longwave channel) and 4.2 (shortwave channel). This example from July 12, 1995, is representative of the comparison of the two systems for the entire period of June 1 through July 27, 1995. A time period of particularly stable atmospheric conditions was chosen in order to perform a long time average of the spectra from each system. The residual difference between the time averaged spectra for the two instruments is a measure of the systematic "error" that existed between the AERI prototype (AERI-00) and the final AERI-01 system. The residual is less than $0.5 \text{ mW}/(\text{m}^2 \text{ sr cm}^{-1})$ in the longwave channel ($500\text{-}1500 \text{ cm}^{-1}$) and less than about $0.05 \text{ mW}/(\text{m}^2 \text{ sr cm}^{-1})$ in the shortwave channel ($2000\text{-}3000 \text{ cm}^{-1}$). Since the AERI-01 system includes substantial enhancements over the prototype system, it is believed that the residual mainly represents uncertainty in the calibration of the prototype (AERI-00) system.

These residual differences are the subject of continuing investigation; however, the size of the difference is within the error estimates given in Section 3 for the uncertainty in the sky FOV correction. For this reason, it is useful to interpret the error estimates given in Section 3 as applying to the entire AERI prototype (AERI-00) operating period April 1994 through July 1995.

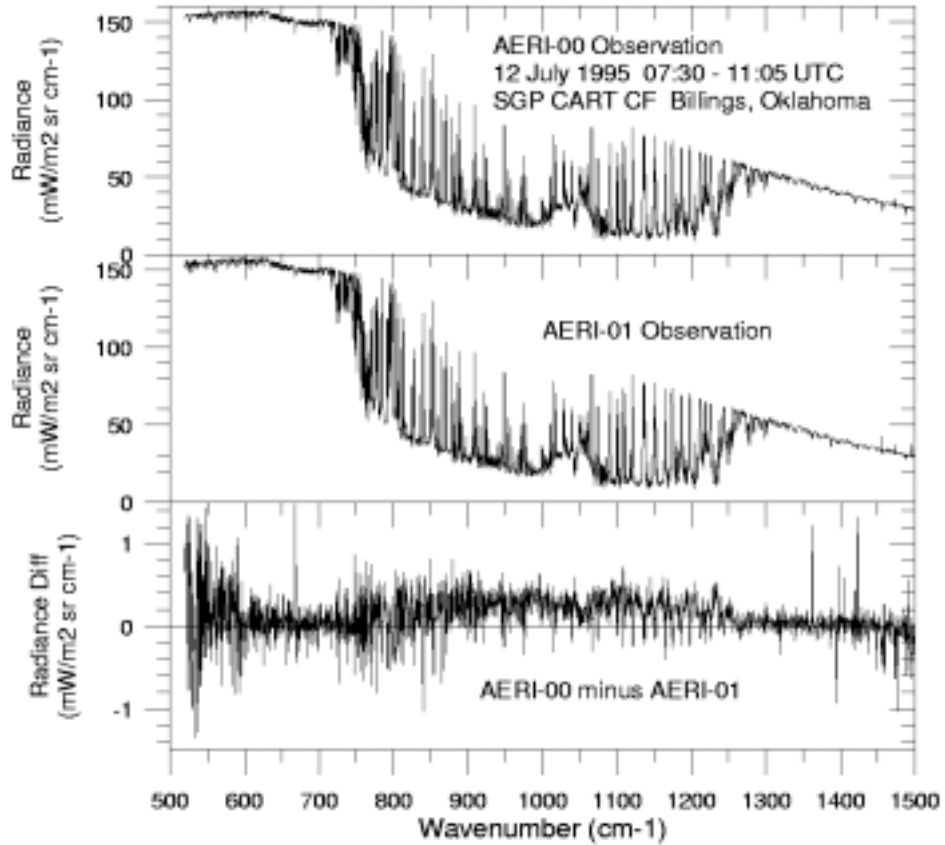


Figure 4.1. Comparison of coincident longwave channel observations of the AERI prototype (AERI-00) and the AERI CF instrument (AERI-01) obtained at the ARM CART site near Billings, Oklahoma. The radiances shown are averages of 26 spectra from each instrument over the time period 07:30 - 11:05 UTC on July 12, 1995. This example is representative of the comparison of the two AERI instruments during the period of intercomparison (June and July 1995) after the obstruction was physically removed from the AERI prototype sky FOV.

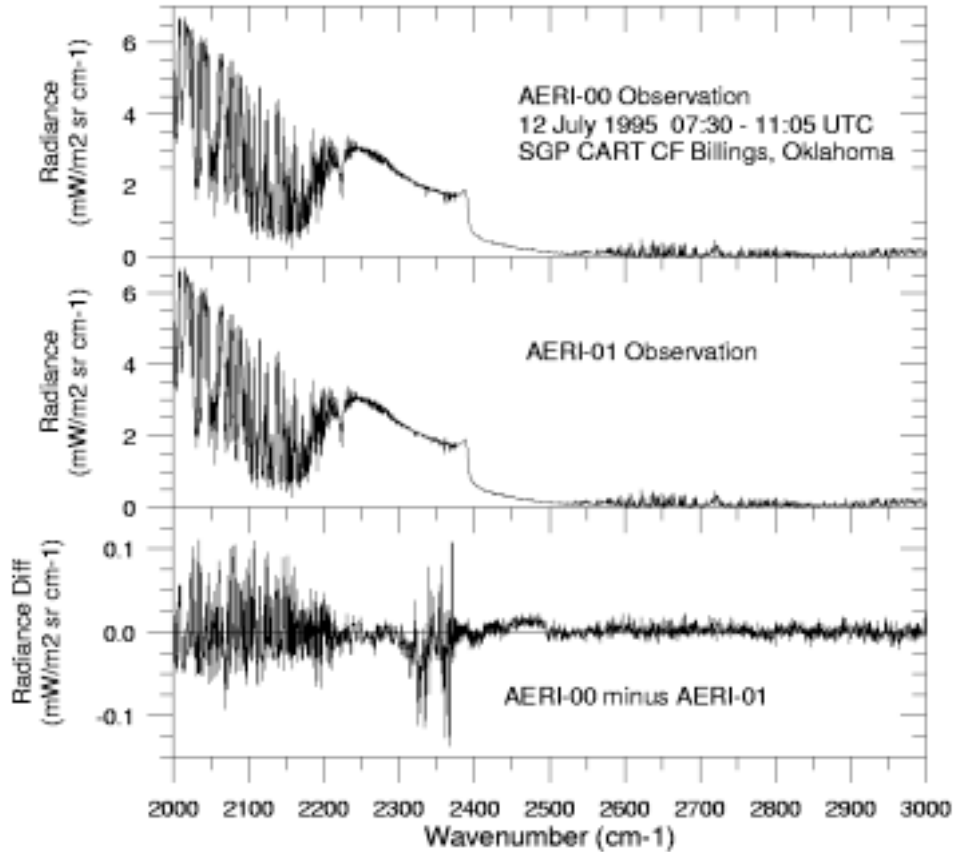


Figure 4.2. Comparison of coincident shortwave channel observations of the AERI prototype (AERI-00) and the AERI CF instrument (AERI-01) obtained at the ARM CART site near Billings, Oklahoma. The radiances shown are averages of 26 spectra from each instrument over the time period 07:30 - 11:05 UTC on July 12, 1995. This example is representative of the comparison of the two AERI instruments during the period of intercomparison (June and July 1995) after the obstruction was physically removed from the AERI prototype sky FOV.